Strong ground motion simulations of the 2016 Kumamoto earthquakes using corrected empirical Green's functions: methods and results for ESG6 blind prediction Steps 2 and 3 with improved parameters

Yosuke Nagasaka[1*]

Abstract

This paper describes the methods and results of the strong ground motion simulations for three earthquakes from the 2016 Kumamoto earthquake sequence using corrected empirical Green's functions. The target earthquakes were an aftershock (M_w 5.5), the largest foreshock of the sequence (M_w 6.1), and the mainshock (M_w 7.1). The corrected empirical Green's function method was used in the simulations. This simulation method combines simple source and path factors with empirical site amplification and phase factors to generate realistic site-specific strong motions. Simulations were originally conducted to participate in blind prediction exercises in ESG6. Although the simulations performed in this study were based on the models submitted to the blind prediction committee, several modifications were made after the blind prediction exercise. First, the observed records at the target site of the blind prediction called KUMA were used to compare observed and synthetic strong ground motions. In addition, a regional spectral inversion was conducted to obtain a more appropriate Q-value and site amplification factor. Synthetic strong motions were found to explain the observed strong ground motions at KUMA and other stations. Comparisons with predictions by other methods and the sensitivity to the rupture scenario were also discussed. These results provide useful information for applying the corrected Green's function method to strong ground motion simulations.

Keywords 2016 Kumamoto earthquake sequence, Strong ground motion simulation, Corrected Green's function method, Spectral inversion, Site amplification factor, Blind prediction
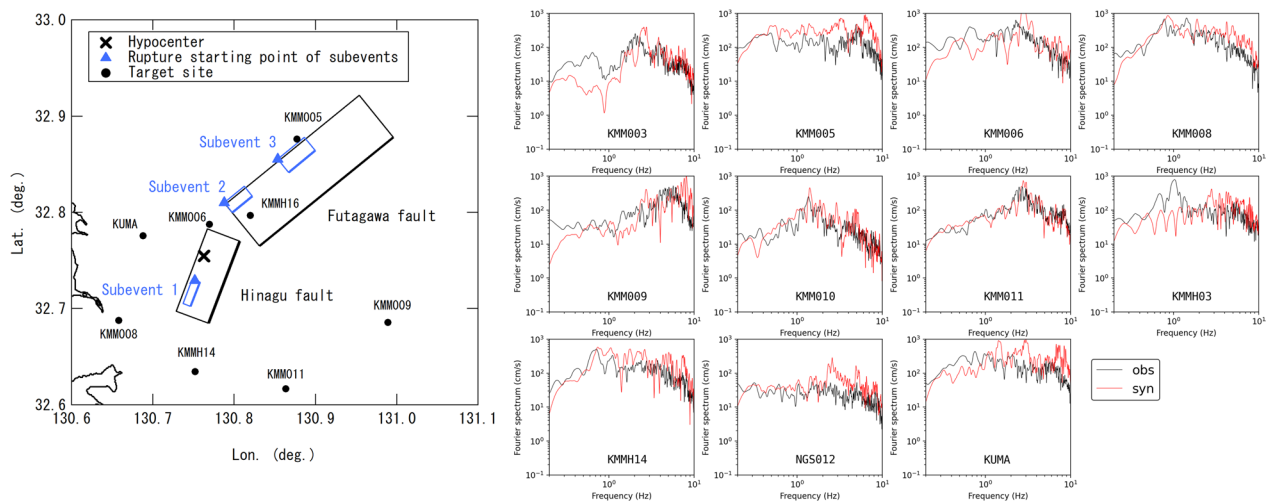
*Correspondence:
Yosuke Nagasaka
nagasaka-y@p.mpat.go.jp
Full list of author information is available at the end of the article

Graphical Abstract

Introduction

In the 6th IASPEI/IAEE International Symposium: The Effects of Surface Geology on Seismic Motion (ESG6) in 2021, a blind prediction exercise for the 2016 Kumamoto earthquake sequence was held (Matsushima et al. 2021). Blind prediction included an estimation of the subsurface structure (Step 1) and estimations of strong motions (Steps 2 and 3) at a designated site (Tsuno et al. 2021a, b; Tsuno et al. 2021b). Step 2 was for a moderate earthquake, and Step 3 was for the largest foreshock and mainshock of the sequence. The author participated in Steps 2 and 3 of the blind prediction to examine the performance of a simulation method called the corrected empirical Green's function (EGF) method (Kowada et al. 1998; Nozu et al. 2006; Nozu et al. 2009; Fernandez et al. 2021).

In this article, we summarize the methods and results of strong ground motion simulations. There were two main differences between the simulations performed in this study and those submitted to the blind prediction committee. First, in this study, the observed records at KUMA were used for parameter determination and comparisons of observed and synthetic strong motions. This is because the strong motion records observed at KUMA were released after the blind prediction exercise. Second, the path and site amplification factors were evaluated using a regional spectral inversion to obtain better simulation results. The inversion scheme was determined to be appropriate for simulation purposes and methods. The source models were modified slightly from those used in the blind prediction

exercises. Thus, the results of this study were not the same as those submitted for the blind prediction.

The conditions of the blind prediction exercises (i.e., those used in this study) are reviewed here. Each step of the blind prediction exercise required participants to submit a time history of ground motion at the target site, called KUMA. An important condition of the blind prediction exercise is that predictions are made for earthquakes that have already occurred. Participants can use the data observed around the target site; thus, we have a relatively good understanding of the source of the target earthquakes. In addition, the committee released strong motion data for 12 small earthquakes at KUMA, which enabled participants to estimate the empirical site factor at KUMA. Information on the subsurface structure and observed records at a neighboring hard rock site have also been released. As a result, various methods, including the 1D/2D/3D methods, empirical/stochastic Green's function methods, the spectral ratio approach, and other approaches, were used by participants (Tsuno et al. 2021a). The availability of earthquake-specific source information distinguishes the blind prediction exercise from predictions of future earthquakes. The latter involves uncertainty owing to a lack of source information. When using a source model for the prediction of future earthquakes, the uncertainty in the rupture scenario, such as locations and parameters of the subevents, must be considered. As reviewed here, information on the predictions was well organized in this study. For example, this type of prediction is often required after a large earthquake when determining the ground motions

at a heavily damaged site to investigate damage mechanisms based on aftershock observations. Considering these conditions, the simulations were performed using as much data as possible. Path and site factors were estimated using a regional spectral inversion. Strong motion data from the source region were used to determine source parameters.

In this study, after our simulation results and their robustness were demonstrated, the performance of our results was compared with those of other participants. Finally, the variability caused by the rupture scenario was examined as a reference for future earthquakes.

Target earthquakes and sites

The 2016 Kumamoto earthquake struck the central area of Kyushu Island in southwestern Japan. The earthquakes in this sequence were mainly hosted by the Futagawa-Hinagu fault zone, and some earthquakes also occurred beneath Aso Caldera, which lies northeast of the Futagawa fault.

The target earthquakes for blind prediction (and this study) are listed in Table 1. The earthquake at 3:03 on April 16, 2016 (JST) is a moderate sized earthquake with M_w 5.5, which occurred at a relatively shallow part beneath Aso Caldera (JST time zone, which is 9 h ahead of UTC, is used throughout this article). The earthquake at 21:26 on April 14, 2016, was the largest foreshock of the sequence. This earthquake is known to have occurred on the Hinagu fault (e.g., Asano and Iwata 2016). The earthquake at 1:25 am on April 16, 2016 (hereafter referred to as the mainshock) was the largest earthquake in the sequence. The rupture of the mainshock began near the bend of the Futagawa-Hinagu fault zone (Sugito et al. 2016) and mainly propagated northeast of the Futagawa fault (e.g., Kubo et al. 2016; Nozu and Nagasaka 2017). The rupture is considered to have reached inside Aso Caldera based on the analysis of crustal deformation and surface ruptures, generating surface ruptures spanning approximately 30 km (e.g., Fujiwara et al. 2016).

The strong motion stations used in this study and the epicenters of the target earthquakes are shown in Fig. 1. All stations other than KUMA are K-NET or KiK-net stations (Aoi et al. 2020). KUMA is located in the Kumamoto Basin, northwest of the epicenter of the mainshock. As
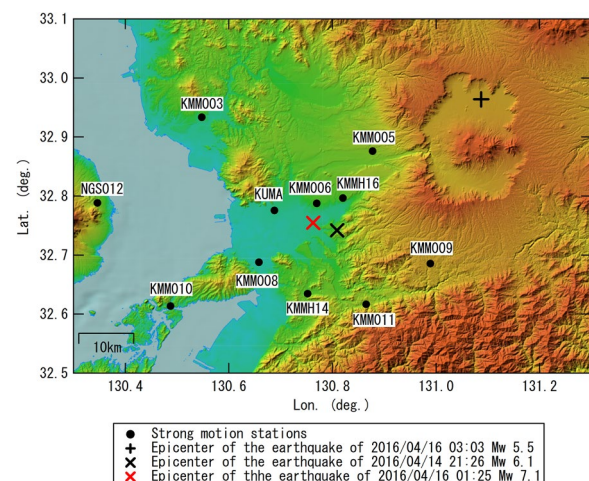
Fig. 1 Locations of target earthquakes and sites used in the simulations. Black dots indicate the target sites. Black plus sign and black and red crosses indicate the epicenters of the earthquakes of 2016/04/16 03:03 (M_w 5.5), 2016/04/14 21:26 (M_w 6.1), and 2016/04/16 01/25 (M_w 7.1), respectively

shown in Fig. 1, KUMA fills the gap between K-NET stations KMM006 and KMM008. Therefore, using KUMA for the simulation contributed to better azimuthal coverage for the simulations. In addition, basin effects are important in strong ground motion studies. Only the surface records were used for the simulations. The target sites of the three simulations differed slightly because of the availability of small earthquake records used as EGFs.

Simulation methods

We used the corrected EGF method to synthesize the time history of the strong motion (Kowada et al. 1998; Nozu et al. 2006; Nozu et al. 2009; Fernandez et al. 2021). Synthetic strong motions obtained using the corrected EGF method consist of four factors: source, path, site amplification, and site phase spectra. The synthetic amplitude spectrum consisted of source, path, and site amplification factors. The synthetic spectrum (Syn(f)) is given by

$$\mathrm{Syn}(f) = \mathrm{Syn}_{\mathrm{amp}}(f)\,\mathrm{Syn}_{\mathrm{phase}}(f),$$

Table 1 List of target earthquakes

Date	M_w*	Depth* (km)	Latitude*	Longitude*	Mechanism* (strike, dip, rake)
2016/04/16 03:03	5.5	6.89	32.9638	131.0868	(209;116, 60;85, − 174; − 30)
2016/04/14 21:26	6.1	11.39	32.7417	130.8087	(122;212, 74;89, − 1; − 164)
2016/04/16 01:25	7.1	12.45	32.7545	130.7630	(131;226, 53;84, − 7; − 142)

*M_w and focal mechanisms were obtained from F-net, depth, latitude, and longitude from the Japan Meteorological Agency (JMA). All times and dates are presented for JST time zone

$$\mathrm{Syn_{amp}}(f) = S(f)P(f)G(f),$$

$$\mathrm{Syn_{phase}}(f) = O(f)/\left|O(f)\right|_p,$$

in which f is the frequency, $\mathrm{Syn_{amp}}(f)$ is the synthetic amplitude spectrum, $\mathrm{Syn_{phase}}(f)$ is the synthetic phase spectrum, $S(f)$ is the source spectrum, $P(f)$ is the path spectrum, $G(f)$ is the site amplification spectrum, $O(f)$ is the Fourier spectrum of a weak motion record at the target site, and $\left|O(f)\right|_p$ is the absolute value of $O(f)$ to which a Parzen window of 0.05 Hz bandwidth is applied. Source, path, and site amplification spectra are real-valued spectra. The phase spectrum is a complex spectrum whose amplitude is almost one with small ripples, which are necessary for satisfying the causality law (Nozu et al. 2009).

The source is modeled by rectangular areas on the fault planes, which are called asperities or subevents. This model assumes that strong motion is generated from part of the fault plane (Kamae and Irikura 1998). In the calculations, the subevents were divided into smaller areas to consider the rupture propagation effect. Strong motions from each divided subevent were summed with appropriate time intervals corresponding to the rupture propagation time. The source spectrum from a divided subevent, which is defined in the dimension of acceleration in this study, is modeled by the omega-square model (Boore 1983), which is given by

$$S(f) = R_{\theta\phi} \cdot \mathrm{PRTITN} \cdot \mathrm{FS} \cdot \frac{M}{4\pi\rho V_S^3} \cdot \frac{(2\pi f)^2}{1 + (f/f_c)^2},$$

in which $R_{\theta\phi}$ is the radiation coefficient, PRTITN is the coefficient to divide the seismic energy into two horizontal components, FS ($= 2$) is the amplification due to the free surface, M is the seismic moment, and f_c is the corner frequency. The average radiation coefficient (0.63) and PRTITN (0.72) were used in this study. The source time function was modeled by Irikura et al. (1997).

A point source is sometimes sufficient to explain the observed strong motions instead of finite rectangular subevents, particularly for small or moderate earthquakes. In this particular case, we did not divide the subevents; thus, the omega-square spectrum represents the source spectrum. This method is called the pseudo point-source model (Nozu 2012). We used the pseudo point-source model in Step 2 and rectangular subevents for the two earthquakes in Step 3.

The path factor includes geometrical spreading and inelastic attenuation (Boore 1983), which is given by

$$P(f) = \frac{1}{r}\exp\left(-\frac{\pi r f}{QV_S}\right),$$

in which r is the distance from the source to the site, Q is the quality factor, and V_S is the S-wave velocity. r was calculated by assuming a straight line. V_s was assumed to be uniform ($= 3.55$ km/s).

The site amplification factor represents the site effect above the seismological bedrock. In the corrected EGF method, empirical site amplification factors, including both direct S-waves and later phases, are used. Later phases refer to the part that comes after the direct S-wave, including both coda and surface waves. These can be evaluated by spectral inversion using full waveforms. The phase spectra of small earthquake records were used as the synthetic phase characteristics. The earthquakes for the phase spectra were selected from foreshocks or aftershocks that occurred close to the target earthquake. In the blind prediction exercise, we selected the EGF from 12 small earthquakes whose records at KUMA were released by the committee.

The nonlinear responses of near-surface layers were considered using a simple method proposed by Nozu et al. (2009), which can be applied to the corrected EGF method. Two parameters that represent the decrease in average S-wave velocity (v_1) and average increase in damping factor(v_2) are used. The synthetic waveforms were corrected as follows.

$$g_n(t_0 + (t - t_0)/v_1) = g(t)\exp(-v_2\omega(t - t_0)),$$

in which $g(t)$ is the synthetic Green's function of the corrected EGF method, $g_n(t)$ is the synthetic Green's function with nonlinear effects, and t_0 is the S-wave arrival time. v_1 works to stretch waveforms after S-wave arrival. v_2 works to attenuate later phases. Summations were conducted after this correction when rectangular subevents were used.

The EGF method (Irikura 1983, 1986; Irikura et al. 1997) uses small earthquake records as the EGF. Conversely, the corrected EGF method uses statistical models for the source and path with empirical site characteristics. Thus, the corrected EGF method generates strong motions consistent with the omega-square source model (Fernandez et al. 2021). While simple statistical models are used for the source and path terms, empirical site amplification and phase factors enable the synthesis of realistic and site-specific ground motions. Because the source and path spectra are both relatively smooth functions of frequency, the frequency dependence of the synthetic spectra is mostly determined by the site amplification factor.
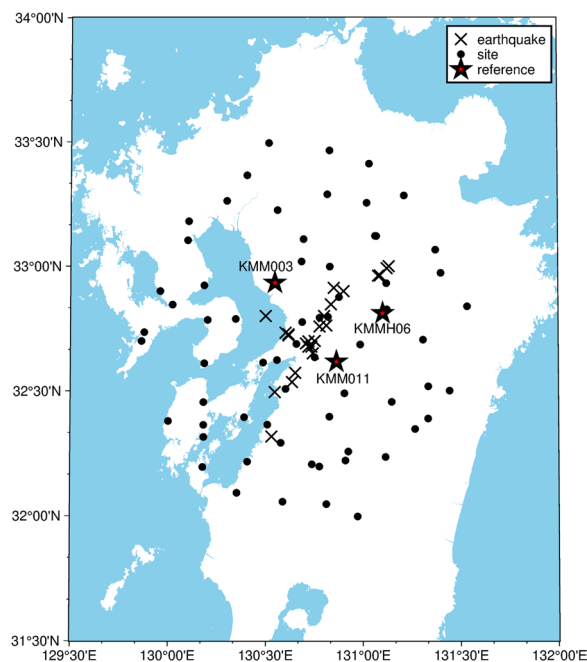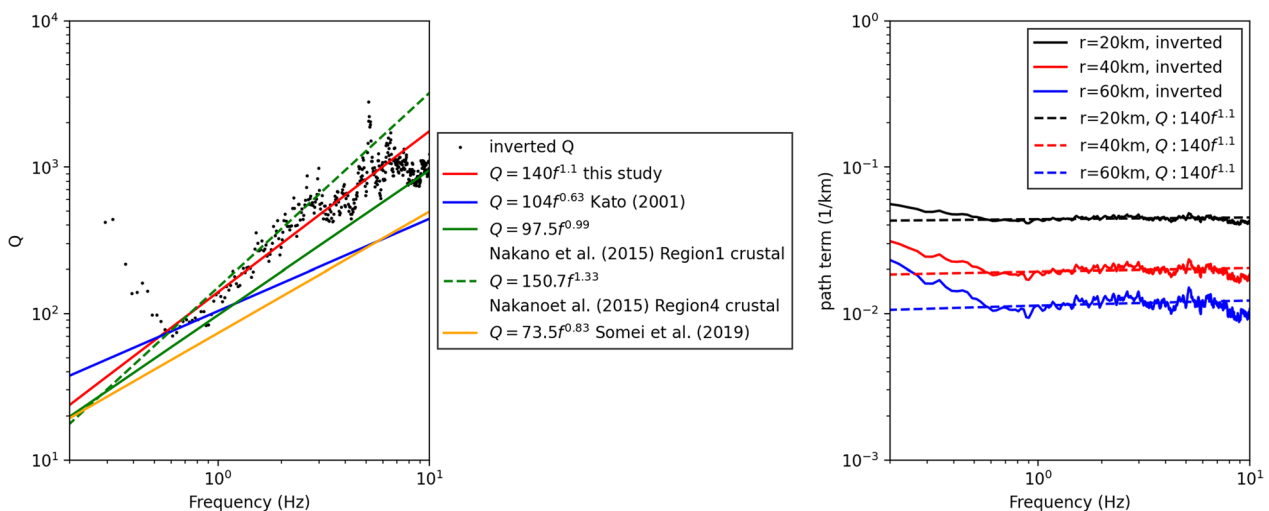
Fig. 2 Earthquakes and sites used in the spectral inversion for Q-value and site amplification factors. Black dots indicate the strong motion stations used in the inversion. Black crosses indicate the epicenters of the earthquakes used in the inversion. Red stars indicate the reference sites of the inversion

observations for small earthquake records. Sometimes, we attempt to estimate strong ground motions after a large earthquake at a severely damaged site. In such cases, short-term aftershock observations are useful for evaluating the site amplification factors. Another option involves the use of microtremor observations. Estimation of site amplification factors from microtremor observations has been studied for practical purposes (e.g., Nishikiori et al. 2019). Recently, the direct estimation of site amplification factors from the microtremor horizontal-to-vertical spectrum was also studied (Pan et al. 2022) using a neural network. Although site-specific phase information cannot be evaluated from microtremors, the situation is better than that without both amplitude and phase information. Thus, empirical site characteristics will become more accessible through the development of these techniques, leading to a wider application of the corrected EGF method.

Source parameters, Q-values, and site amplification factors are required to synthesize the ground motions using the corrected EGF method. In this study, source parameters were determined to explain the recorded strong motions of the target earthquakes. The Q-value and site amplification factors were evaluated using spectral inversion of strong motion records.

One limitation of EGF-based methods is that weak motion records are necessary for the simulation. This limitation may be mitigated by short-term earthquake

Fig. 3 Inverted Q-value and behavior of the path factor. (Left) Black dots indicate the inverted Q-values by the spectral inversion. The red line indicates the linear approximation of the inverted Q-value. Blue, green, green dashed, and yellow lines indicate the Q-values estimated in the area around the Kumamoto earthquakes by Kato (2001), Nakano et al. (2015) in Region 1 for crustal earthquakes, Nakano et al. (2015) in Region 4 for crustal earthquakes, and Somei et al. (2019), respectively. In Nakano et al. (2015), Region 1 includes the west of Kyushu Island and Region 4 includes the east of Kyushu Island. (Right) Black, red, and blue lines indicate the frequency dependence of the path term by the inverted Q-value at distances of 20, 40, and 60 km, respectively. Black, red, and blue dashed lines indicate the frequency dependence of the path term by $Q = 140f^{1.1}$ at the distance of 20, 40, and 60 km, respectively
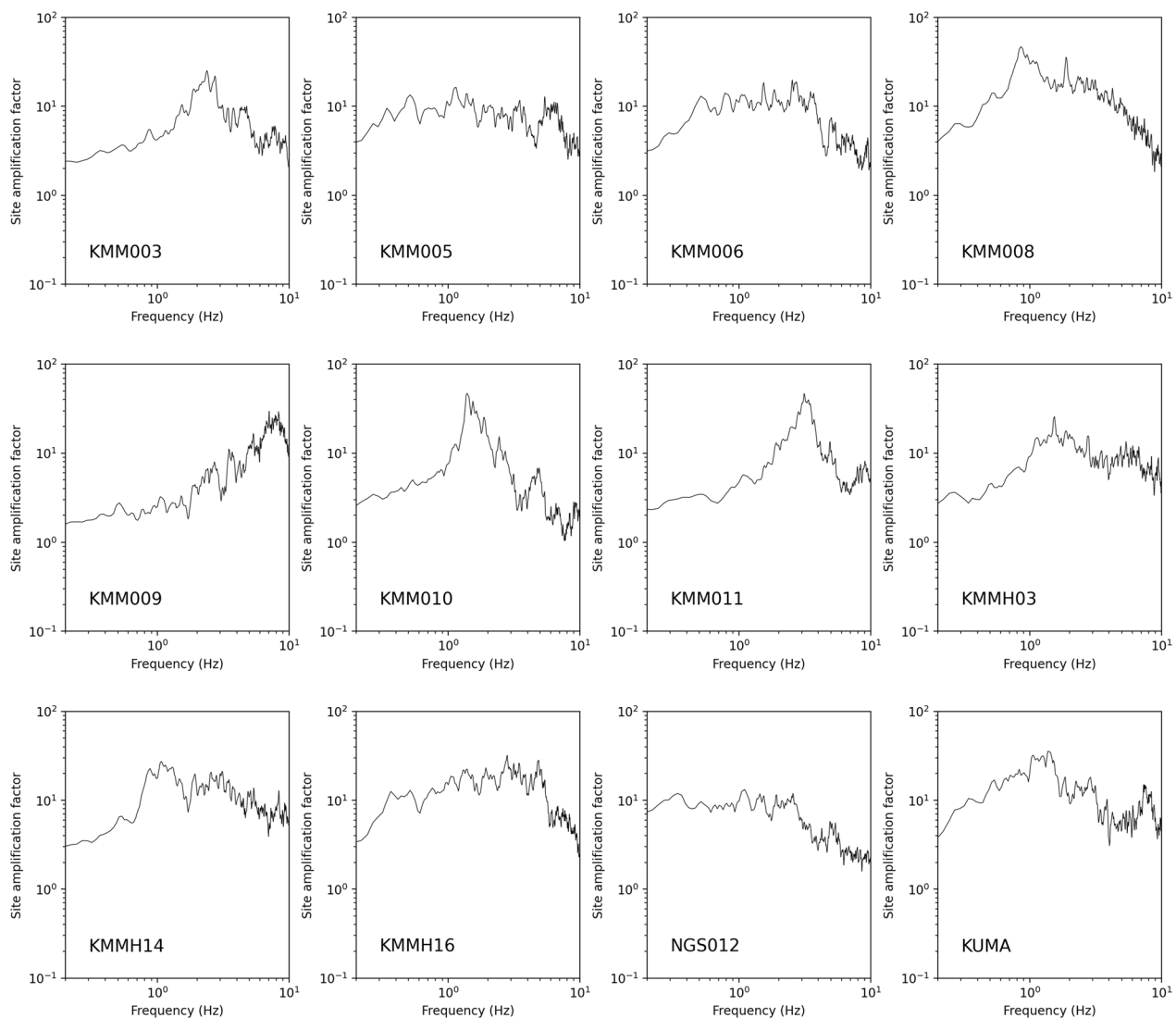
Fig. 4 Inverted site amplification factors. Black lines indicate the site amplification factors estimated by the spectral inversion in this study

Table 2 Parameters of the simulation for the earthquake of 2016/04/16 03:03 (M_w 5.5)

Point source coordinates[*]	Latitude: 32.9638° Longitude: 131.0868° Depth: 6.89 km
Seismic moment	0.6E + 17 Nm
Corner frequency	0.4 Hz
Earthquake for the phase characteristics and its mechanism (strike, dip, rake)[*]	2016-04-17 00:14 (M_J 4.8) (241, 54, − 161)

[*]From F-net

Evaluation of *Q*-value and site amplification factors

The *Q*-value and empirical site amplification factors were necessary to apply the corrected EGF method. Spectral inversion using recorded ground motion is a widely used method for simultaneously evaluating these factors. This method separates observed strong motion spectra into source, path, and site factors (e.g., Castro et al. 1990; Nakano et al. 2015; Shible et al. 2022). The main advantage of spectral inversion for evaluating the site amplification factor is that it can evaluate the average factor from various earthquake locations over a wide frequency range without knowledge of the subsurface structure.

Spectral inversion was applied to evaluate the path and site amplification factors at sites in the Kumamoto area. The selection of the inversion scheme and data is important and should be appropriate for our purposes, which is to use the estimated path and site factors in strong ground motion simulations. Thus, we first
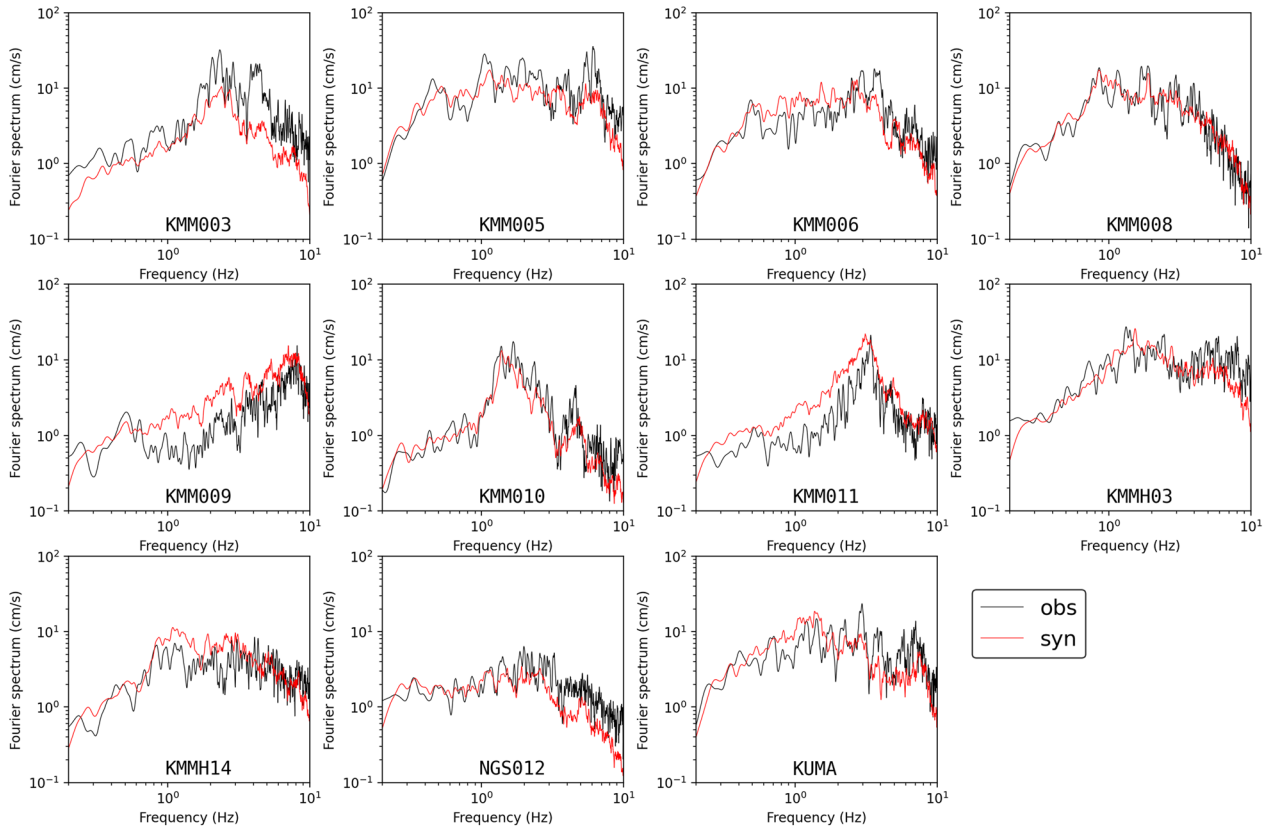
Fig. 5 Synthetic and observed Fourier spectra for the earthquake of 2016/04/16 3:03 (M_w 5.5). Black lines indicate the observed Fourier spectra. Red lines indicate the synthetic Fourier spectra

selected records from the 2016 Kumamoto earthquake sequence and records of epicentral distances within 80 km. This was intended to focus on the Kumamoto area and mitigate the effects of the heterogeneous attenuation characteristics. Second, we used full waveforms, including the later phases, for the inversion. Although some previous studies have evaluated the Q-value and site amplification factors in the Kumamoto area (e.g., Kato 2001; Somei et al. 2019), only the S-wave has been used for the inversion. Later phases are important for simulations, especially at sites in sedimentary basins, such as KUMA. A two-step scheme was adopted for the full waveforms (Nozu et al. 2006; Nakano et al. 2015). In the first step, only the S-wave was used to evaluate the source and path factors of the S-wave. In the second step, the Fourier spectra of the full waveforms were divided by the S-wave source and path factors to obtain the site factors, including the effects of later phases. In this study, we adopted a one-step inversion with full waveforms using reference site factors evaluated using a two-step scheme. The observed Fourier spectra were modeled as follows:

$$O_{ij}(f) = S_i(f)\frac{1}{r_{ij}}\exp\left(-\frac{\pi f r_{ij}}{QV_S}\right)G_j(f)\varepsilon_{ij}(f),$$

in which i is the earthquake index, j is the site index, O_{ij} is the observed Fourier amplitude spectrum including later phases, S_i is the source spectrum, r_{ij} is the distance from ith earthquake to jth site, G_j is the site amplification factor, and ε_{ij} is the residual term. Iwata and Irikura (1986) first used this model. The path factor was modeled to be consistent with the corrected EGF method. Taking the logarithm of this equation yields

$$\log O_{ij} = \log S_i - \left(\log r_{ij} + \frac{\pi f r_{ij}}{QV_S}\right) + \log G_j + \log \varepsilon_{ij}.$$

The unknown parameters were S_i, G_j, and Q. A uniform Q-value was assumed. Using observed records from many earthquakes and sites to form a linear system of observation equations, unknown parameters can be evaluated by the least-squares approach that minimizes the square sum of $\log \varepsilon_{ij}$. $Vs = 3.55$ km/s, which was used in the analysis by F-net (Aoi et al. 2020), was used here.
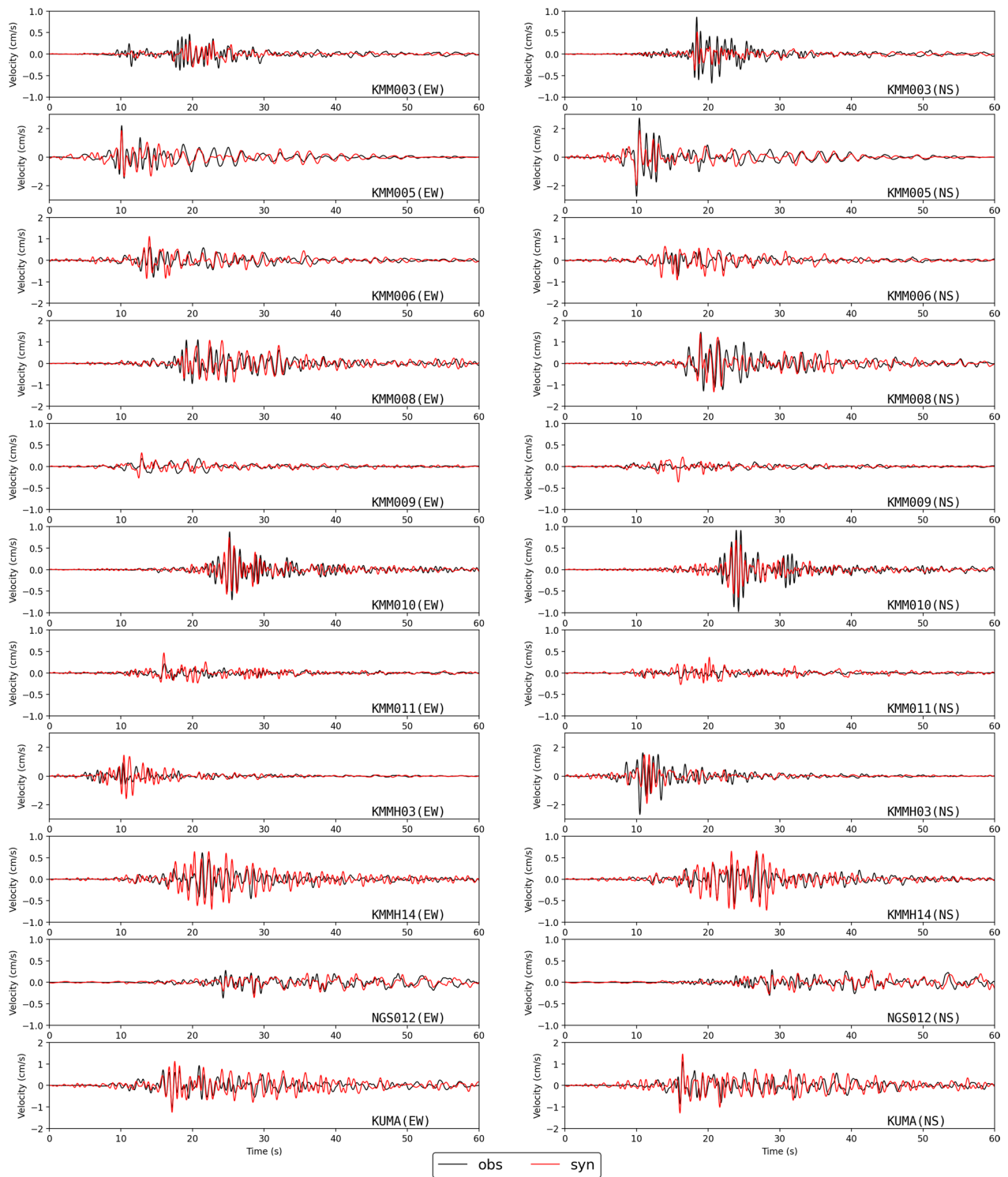
Fig. 6 Synthetic and observed velocity time histories (0.2–2 Hz) for the earthquake of 2016/04/16 03:03 (M_w 5.5). Black lines indicate the observed velocities. Red lines indicate the synthetic velocities

Table 3 Simulation parameters for the earthquake of 2016/04/14 21:26 (M_w 6.1)

	Subevent 1	Subevent 2
Strike	212°	
Dip	89°	
Seismic moment	0.3E + 18 Nm	0.2E + 18 Nm
Rupture propagation velocity inside asperity	2.5 km/s	2.5 km/s
Rise time	0.5 s	0.5 s
Length and width	3 km, 3 km	3 km, 3 km
Number of divisions (along strike, along dip, time)	(4, 4, 4)	(4, 4, 4)
Relative rupture time	0.0 s	3.0 s
Earthquake for the phase characteristics (strike, dip, rake)*	2016-04-16 11:02 (M_J 4.4) (199, 41, − 102)	

*From F-net

To avoid tradeoffs between the source and site factors, we provided reference site factors at three sites (KMM003, KMM011, and KMMH06) estimated by Nozu et al. (2006). Nozu et al. (2006) evaluated site amplification factors, including the effects of later phases. Some stations were relocated after 2006 and KUMA was not included in Nozu et al. (2006). A fixed Q-value for Kyushu Island was used in Nozu et al. (2006). Therefore, we evaluated the updated site and path factors, focusing on the Kumamoto area.
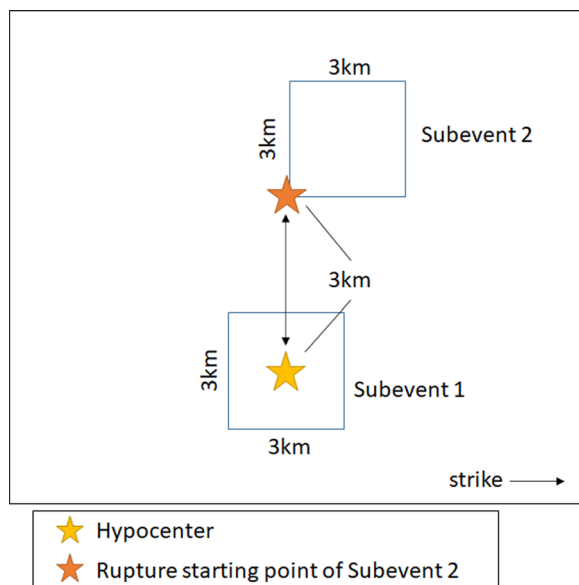
Fig. 7 Subevents of the reference case for the earthquake of 2016/04/14 21:26 (M_w 6.1). Blue rectangles indicate the subevents used for the simulation. The black rectangle represents the fault plane, which is shown only for reference and not considered in the simulation. The yellow star indicates the hypocenter of the target earthquake and the rupture starting point of subevent 1. The orange star indicates the rupture starting point of subevent 2

Using reference site factors from Nozu et al. (2006), the site factors estimated by a one-step approach using full waveforms are expected to be equivalent to those estimated by the two-step approach. We confirmed that the site factors estimated in this study were almost the same as those reported by Nozu et al. (2006) for stations without relocation. It should be noted that all distance-dependent parts of the observed strong motions were modeled by $P(f)$ because $P(f)$ is the only term that includes distance.

After checking the signal-to-noise ratio of each record, we selected 805 records from 68 stations and 25 earthquakes ($4.5 \leq M_J \leq 6.0$, where M_J is the magnitude scale defined by JMA), as shown in Fig. 2. We excluded records with a peak ground acceleration over 100 Gal to avoid nonlinear effects. The target frequency range is 0.2–10 Hz. The estimated path and site factors are shown in Figs. 3 and 4, respectively. The estimated Q-value could be approximated as $Q = 140f^{1.1}$ above 0.6 Hz and was unstable at lower frequencies. Figure 3 shows the Q-values from previous studies and the behavior of the path factor calculated from the estimated Q-value. The path factor was almost constant at frequencies above 1 Hz and gradually increased at lower frequencies. In the following simulations, we use the inverted Q-value without approximation.

Results

Earthquake of 2016/04/16 03:03 (M_w 5.5)

We used the pseudo point-source model as the source model for the earthquake. The source parameters are listed in Table 2. The point source was placed at the hypocenter. The corner frequency and seismic moment were determined based on the Fourier spectrum (FS) error defined by the following equation:

$$FSerror = \int_{0.2Hz}^{10Hz} \left\{ \log\left(Syn(f)/Obs(f) \right) \right\}^2 d(\log f),$$
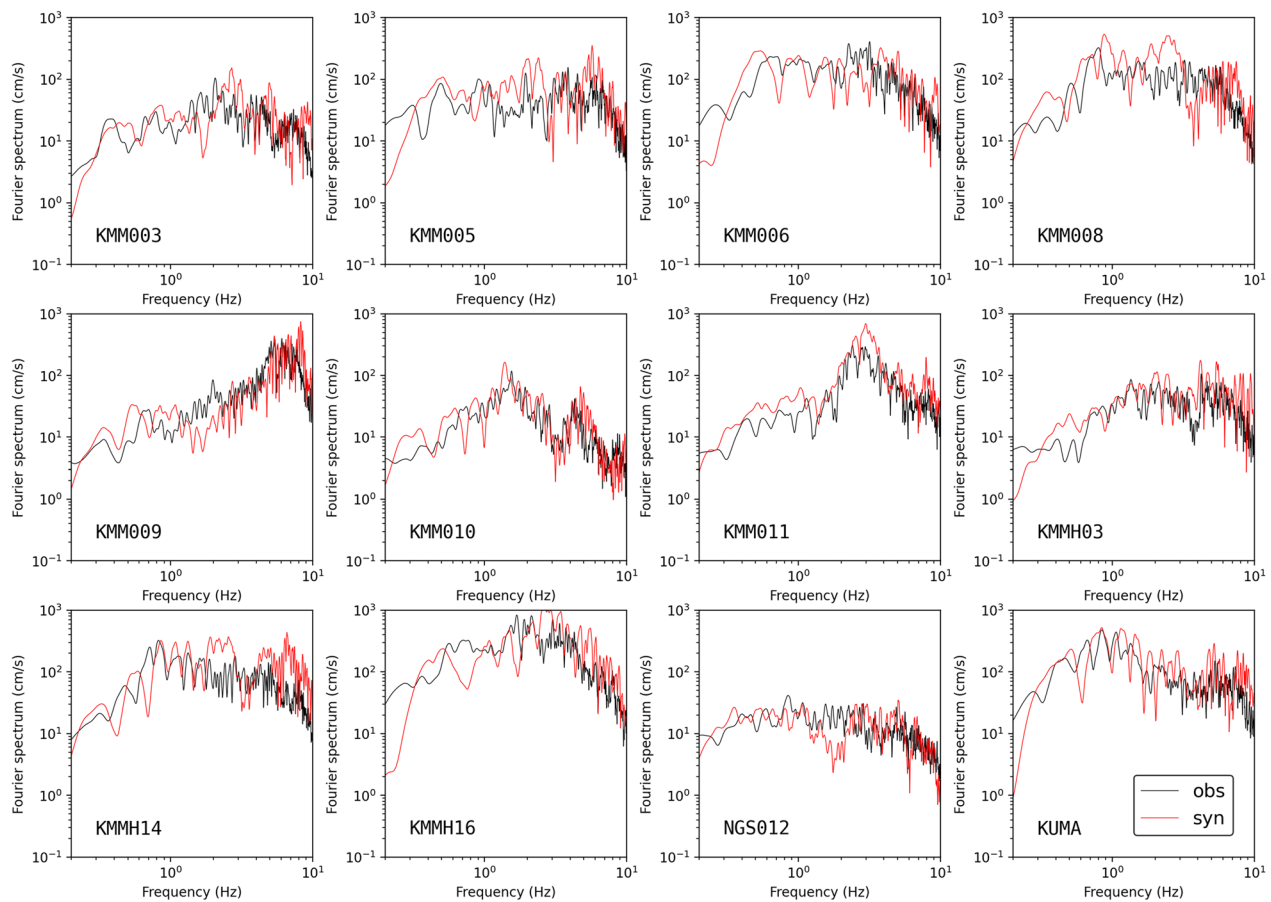
Fig. 8 Synthetic and observed Fourier spectra of the reference case for the earthquake of 2016/04/14 21:26 (M_w 6.1). Black lines indicate the observed Fourier spectra. Red lines indicate the synthetic Fourier spectra

in which $Obs(f)$ represents the observed Fourier spectrum. The Fourier amplitude spectra were used to evaluate the misfit in the corrected EGF method. This is because the phase characteristics of synthetic strong motions were mostly determined by those of small events, which do not necessarily coincide with the phase characteristics of the target earthquake due to the limited number of available small events. The average FS error was calculated from the sites shown in Figs. 5 and 6 and the parameters that minimized the average FS error were identified. The small event for the phase characteristics was the earthquake that occurred closest to the target earthquake among the events released by the committee. The fault mechanisms of the target earthquake and the EGF event were similar as shown in Table 2. Q-value and site amplification factors are shown in Figs. 3 and 4, respectively. The epicenter and target site locations are shown in Fig. 1.

The synthetic and observed acceleration Fourier spectra and velocity time histories (0.2–2 Hz) are compared in Figs. 5 and 6, respectively. These figures generally

show good agreement with the observations and synthetics for both the amplitude and phase characteristics. The synthesized spectra of KMM009 and KMM011 overestimated the observed spectra. These two stations are located in almost the same direction from the hypocenter, as shown in Fig. 1. A possible reason for this overestimation is that a low-Q zone exists under Aso Caldera, and seismic waves to the southwest might be strongly attenuated by this zone. The long duration at KUMA was well simulated by empirical site amplification and phase characteristics, as shown in Fig. 6.

Earthquake of 2016/04/14 21:26 (M_w 6.1)

Rectangular subevents were used as source models for the second target earthquake. The parameters and layout of the subevents were determined as shown in Table 3 and Fig. 7. As shown in Fig. 7, the rupture starting point of subevent 1 was the hypocenter (latitude: 32.7417 deg°, longitude: 130.8087°, depth: 11.39 km). Only increase in the damping factor (v_2) was considered as the nonlinear effect. v_2 was 0.02 for KMM006 and 0.01 or lower for
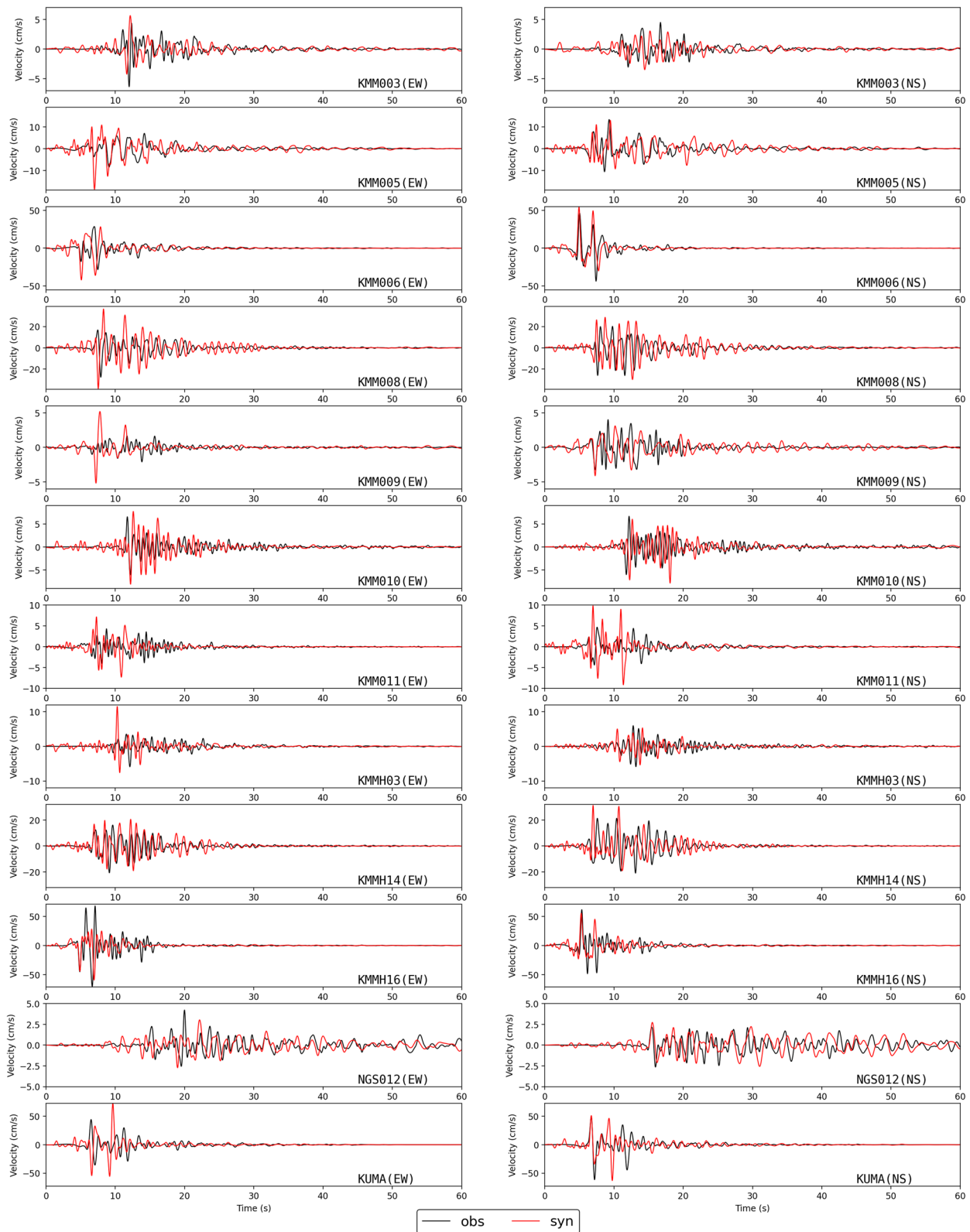
Fig. 9 Synthetic and observed velocity time histories (0.2–2 Hz) of the reference case for the earthquake of 2016/04/14 21:26 (M_w 6.1). Black lines indicate the observed velocities. Red lines indicate the synthetic velocities
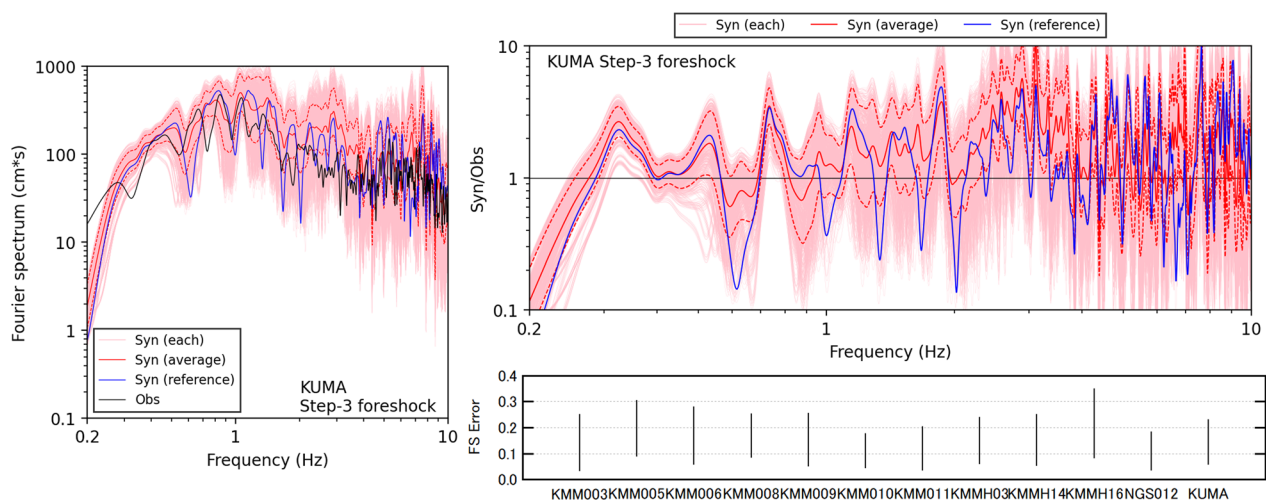
Fig. 10 Variation of the predicted Fourier spectrum at KUMA for the foreshock. (Left) Pink lines indicate the synthetic Fourier spectra of cases that showed better average FS errors than the reference case. The red line indicates the geometric mean of pink lines. The blue line indicates the synthetic Fourier spectrum of the reference case. The black line indicates the observed Fourier spectrum. (Upper right) Pink, red, and blue lines indicate the spectral ratios of the lines of same type in the left panel to the observed spectrum. (Bottom right) Black lines indicate the ranges of FS error at each site

Table 4 Parameters of the earthquake of 2016/04/16 01:25 (M_w 7.1)

	Subevent 1	Subevent 2	Subevent 3
Strike*	205°	235°	235°
Dip*	72°	60°	60°
Seismic moment	0.4E + 18 Nm	0.3E + 18 Nm	1.0E + 18 Nm
Rupture propagation velocity	2.5 km/s	2.5 km/s	2.5 km/s
Rise time	0.5 s	0.3 s	0.8 s
Length and width	3 km, 3 km	3 km, 3 km	4 km, 4 km
Number of divisions (along strike, along dip, time)	(3, 3, 3)	(3, 3, 3)	(4, 4, 4)
Relative rupture time from the origin time	0.0 s	1.0 s	3.5 s
Small earthquake for phase spectra (strike, dip, rake)**	2016-04-17 04:46 (M_J 4.5) (181, 82, 150)	2016-04-21 21:52 (M_J 4.0) (262, 78, − 26)	2016-04-21 21:52 (M_J 4.0) (262, 78, -26) or 2016-04-18 08:35 (M_J 4.2) (98, 61, − 112)***

* Strike and dip angles were obtained from an analysis of crustal deformation by the Geospatial Information Authority of Japan (GSI) (see Availability of Data and Materials for details)

** From F-net

*** The earthquake of 2016-04-21 21:52 was used at KMM008, KMMH14, and NGS012 because of the availability of the observed data. The earthquake of 2016-04-18 08:35 was used at other sites

the other sites. A small ν_2 value slightly attenuates later phases. The path and site amplification factors are shown in Figs. 3 and 4, respectively. The small event for the phase characteristics was the earthquake that occurred closest to the hypocenter. Two subevents were used for the simulation to explain the two pulse-like waveforms clearly observed in the velocity waveforms—for example, at KMM006. However, it was difficult to identify the subevent locations that provided the perfect arrival times of

the pulse-like waveforms for all sites. Thus, the locations and relative rupture times of the subevents were determined primarily by referring to KMM006 and KMMH16, in which the two pulse-like waveforms were clear. The rupture starting points of the subevents were determined by considering the directivity effect. The rupture of subevent 2 propagates southward. If the rupture of subevent 2 propagated northward, the synthetic strong motions were underestimated at KMMH14 and overestimated at
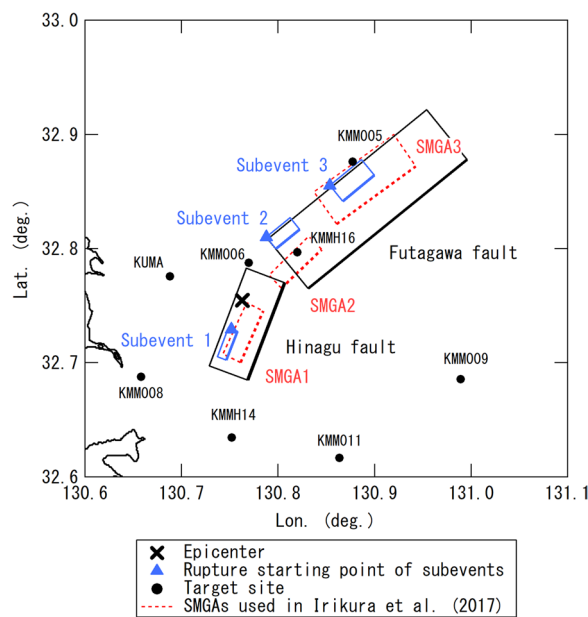
Fig. 11 Location of reference case subevents for the earthquake of 2016/04/16 01:25 (M_w 7.1). Blue rectangles indicate the projections of subevents used for the simulation. Projections of the Hinagu and Futagawa faults were estimated by Geospatial Information Authority of Japan, which are shown only for reference and not considered in the simulation. Blue triangles indicate the rupture starting points of the subevents. Red dashed rectangles indicate SMGAs used in Irikura et al. (2017) shown only for reference. Black dots indicate the target sites of the simulation

KMM006 and KMMH16. There are still a large number of combinations of parameters that give similar average FS errors. In this section, we first present the results of the reference case whose parameters were determined using a trial-and-error approach. The robustness of the prediction at KUMA was then examined based on the results of many cases that showed better average FS errors than the reference case. Table 3 lists the parameters of the reference case. For the reference case, the seismic moments of subevents 1 and 2 were assumed to be $0.3E+18$ and $0.2E+18$ Nm, respectively, based on the fitting of the low-frequency Fourier spectra and the amplitudes of the velocity pulses. The area, rupture velocity inside the subevent, and rise time were assumed to be common to the two subevents because the durations of the two pulses were almost identical in the observed velocities. In terms of the corner frequency of the source spectrum, the size and rupture velocity exhibit a tradeoff. The rupture velocity was fixed at 2.5 km/s, which is about $0.7V_s$. Then, the size and rise time were determined based on the general reproducibility of the Fourier spectra and velocity waveforms. The number of divisions was determined based on Fourier spectrum fitting to limit destructive summations from the divided subevents.

The observed and synthetic acceleration Fourier spectra and velocity time histories (0.2–2 Hz) of the reference case are compared in Figs. 8 and 9, respectively. Figures 8 and 9 show that the main features of the observed strong motions were well explained by the synthetics.

Although good agreement is shown in Figs. 8 and 9, the synthetic velocity pulse from subevent 2 at KUMA arrived slightly earlier than the second pulse at the observed velocity. However, the arrival times of two velocity pulses are well explained at neighboring stations, such as KMM006 and KMMH16. Using three subevents (Goto et al. 2019) could improve the arrival times; in fact, observations of some sites (for example, KMM011 and KMMH14) seem to have more than two pulses. In this study, we used two subevents, considering the two clear pulses observed at KMM006 and KMMH16. Opposite polarities of the first S-wave pulse were observed in the observed and synthetic velocities, for example, in KMM008 NS, KMM011 EW and NS, and KUMA EW. This discrepancy may be related to the mechanisms of the EGF and target earthquakes. The target earthquake occurred on a strike-slip fault, and the EGF event occurred on a reverse fault. This is one of the limitations of this study because the choice of EGF events was limited to the 12 earthquakes released by the committee.

The reference case is one of the realizations among many solutions that yield similar FS errors and is not the best solution. Examining the robustness of the prediction at KUMA will be helpful for evaluating the performance of the corrected EGF method for post-earthquake prediction problems. The parameter sets that yielded better average FS errors than the reference case were searched by varying the parameter around the reference case. The FS error at KUMA was not used to examine predictability. The parameters were varied with the following ranges: The seismic moments of subevents 1 and 2: [$0.2E+18$ Nm, $0.3E+18$ Nm, $0.4E+18$ Nm]. The rupture velocities inside the subevent: [2.3 km/s, 2.5 km/s, 2.7 km/s]. The lengths (widths) of subevents 1 and 2: [2 km, 3 km, 4 km]. The rise time: [0.4 s, 0.5 s, 0.6 s]. The numbers of divisions: [3, 4, 5]. The seismic moment and length (and width) of subevents 1 and 2 varied independently, and the other parameters were assumed to be common to both subevents. Total of 2187 ($=3^7$) cases were considered, of which 827 showed better average FS errors than the reference case. The minimum average FS error was 0.095. The average FS error of the reference case was 0.132. The synthetic Fourier spectra at KUMA for these cases as well as for the reference case are shown in Fig. 10. The variation in the synthetic Fourier spectra was within a factor of 1.5–2. This value depends on the permissible FS error range (0.095–0.132 here) and should be regarded as an example value. Figure 10 also illustrates
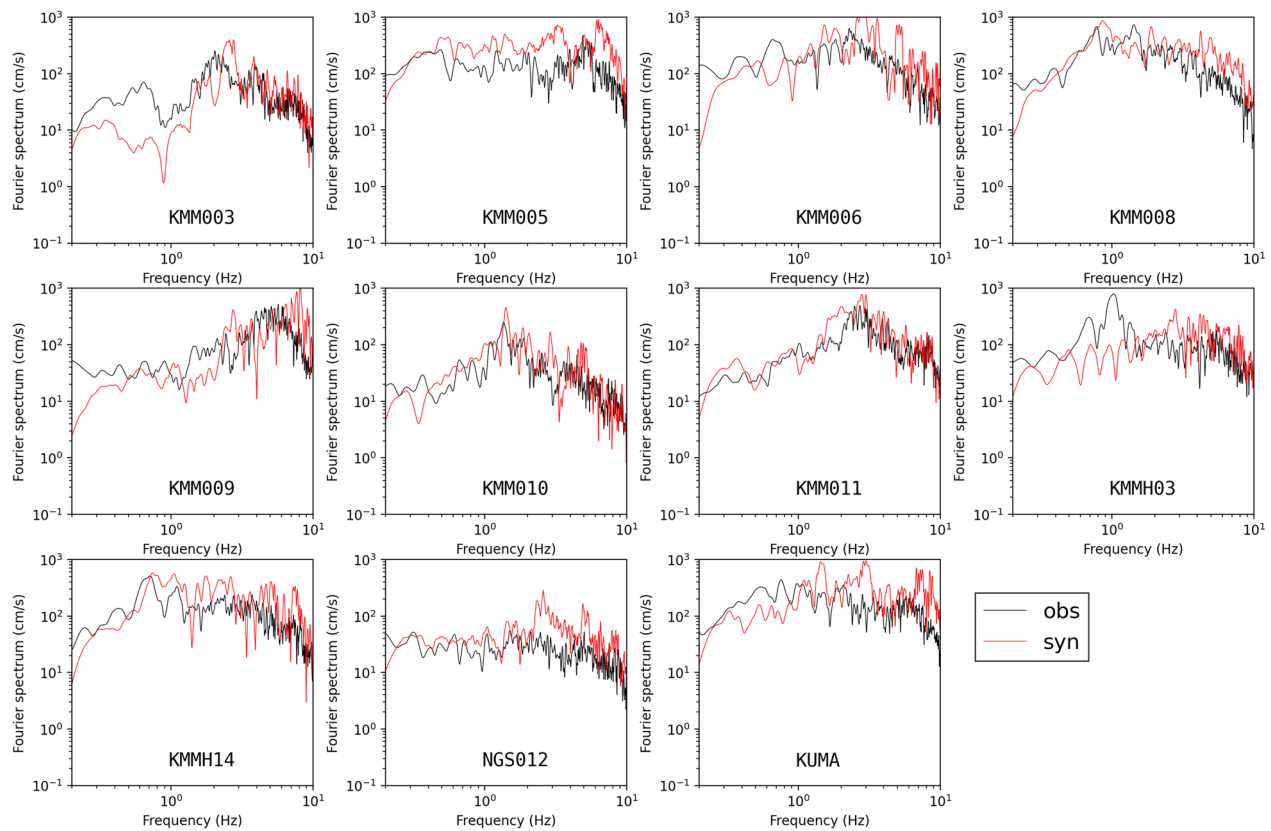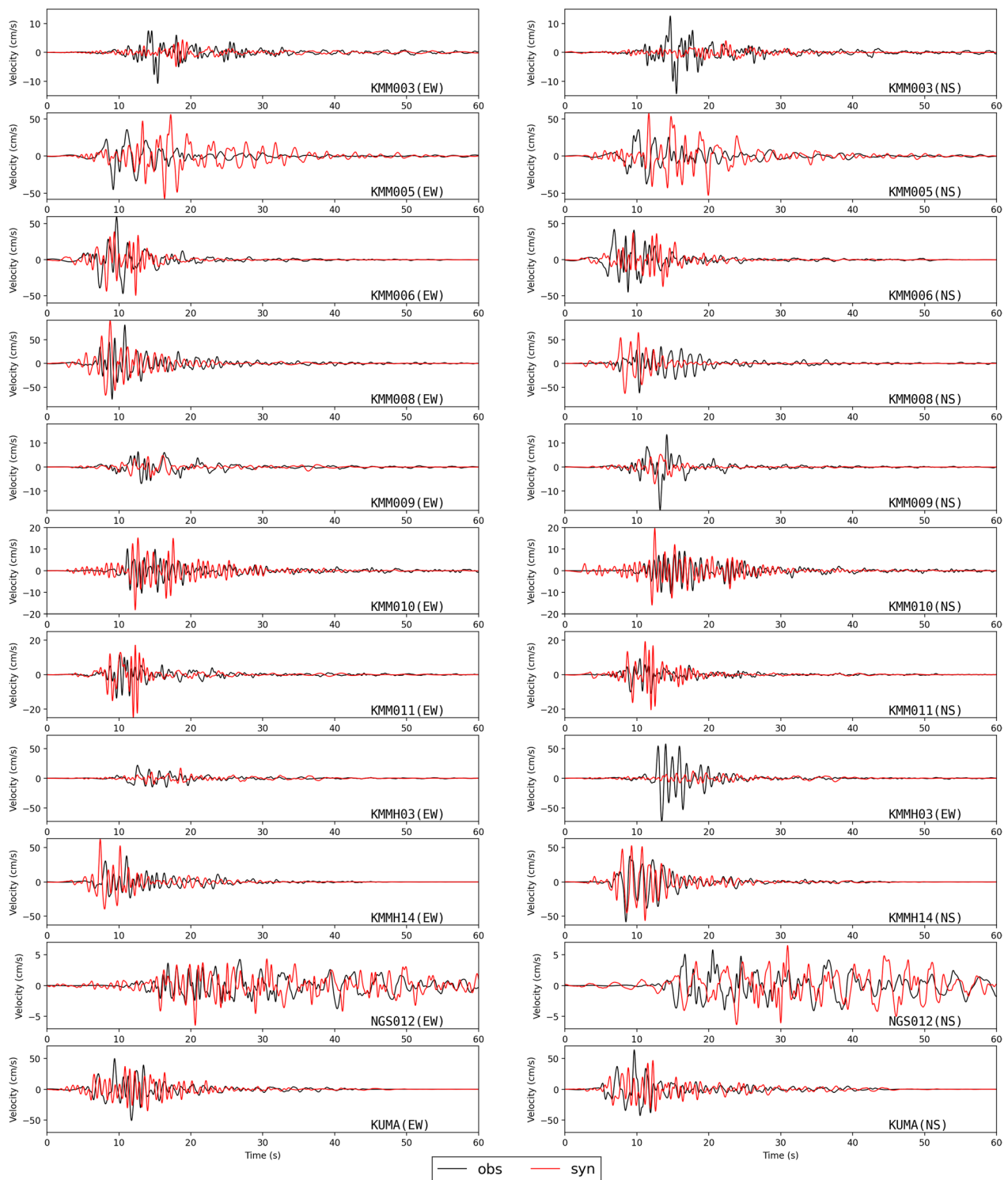
Fig. 12 Synthetic and observed Fourier spectra of the reference case for the earthquake of 2016/04/16 01:25 (M_w 7.1). Black lines indicate the observed Fourier spectra. Red lines indicate the synthetic Fourier spectra

that the reference case was not a special case tuned for KUMA. The ranges of the FS error for the 827 cases are also shown in Fig. 10, indicating that the uncertainty of the prediction at KUMA is comparable to that at other sites. If the parameters are further constrained by other information in addition to the FS error, more robust predictions can be achieved.

Earthquake of 2016 04/16 01:25 (M_w 7.1)
For the mainshock, rectangular subevents were used for the source model. The parameters and layout of the subevents were determined as shown in Table 4 and Fig. 11. Table 4 lists the parameters of the reference case as in Table 3 for the foreshock. Three subevents were used to simulate the mainshock. The locations of these subevents are generally consistent with those of the three SMGAs used by Irikura et al. (2017). Although subevent 2 and SMGA2 by Irikura et al. (2017) did not overlap, their depths were both approximately 10 km, as shown in Fig. 11. For the nonlinear effects, only increase in the damping factor (ν_2) was considered. ν_2 was 0.01 or less for all target sites. A small ν_2 value slightly attenuates later phases. The path and site amplification factors are shown

in Figs. 3 and 4, respectively. One important factor that was not considered in this study is near-surface rupture. It is known that approximately 30 km of surface ruptures appeared after the mainshock (Fujiwara et al. 2016). Strong velocity pulses exceeding a peak ground velocity of over 100 cm/s were observed at stations near-surface ruptures and caused severe structural damage (Kawase et al. 2017). Near-surface ruptures were considered to have generated strong velocity pulses at these stations, although the contributions of near-surface ruptures were relatively small at KUMA. Thus, the locations and rupture times of the subevents were mainly determined by referring to sites that were not too close to the surface ruptures (e.g., KMM008, KMM010, KMM011, and KMMH14). The ruptures of the subevents were assumed to start from the point closest to the hypocenter. The trial-and-error process was performed in the same manner as that for the foreshock. For the mainshock, the Fourier spectra and phase characteristics at KMM010, KMM011, and KMMH14 were mainly referred to for their good fit with the observed waveforms. The largest slip by kinematic source inversion (Nozu and Nagasaka 2017) lies on the Futagawa fault and ranges from

Fig. 13 Synthetic and observed velocity time histories (0.2–2 Hz) of the reference case for the earthquake of 2016/04/16 01:25 (M_w 7.1). Black lines indicate the observed velocities. Red lines indicate the synthetic velocities
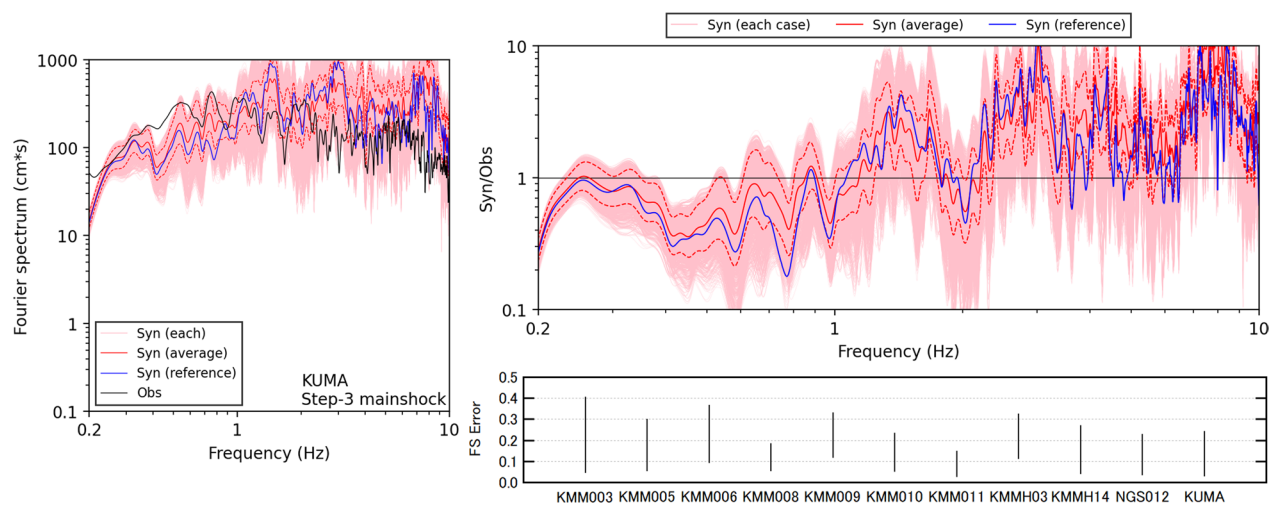
Fig. 14 Variation of the predicted Fourier spectrum at KUMA for the mainshock. (Left) Pink lines indicate the synthetic Fourier spectra of cases that showed better average FS errors than the reference case. The red line indicates the geometric mean of pink lines. The blue line indicates the synthetic Fourier spectrum of the reference case. The black line indicates the observed Fourier spectrum. (Upper right) Pink, red, and blue lines indicate the spectral ratios of the corresponding lines in the left panel to the observed spectrum. (Bottom right) Black lines indicate the ranges of FS error at each site

KMM006 to KMM005. This area was covered by two subevents (2 and 3). Smaller slips on the Hinagu fault by inversion are consistent with the smaller seismic moment of subevent 1, as shown in Table 4. The EGF events for the phase characteristics were earthquakes that occurred close to each subevent. The mechanisms of the EGF events are not consistent with those of the mainshock. As mentioned earlier, this is a limitation due to the availability of EGF events. The selection of EGF events has little effect on the Fourier spectrum, although discrepancies in the phase characteristics, such as opposite polarity, can occur.

The observed and synthetic acceleration Fourier spectra and velocity time histories (0.2–2 Hz) are compared in Figs. 12 and 13, respectively. KMMH16 was not included in the simulation because small earthquake records for the phase spectra were not available. Figures 12 and 13 show that the general features of the observed strong motions were well reproduced by the synthetic results, particularly in the Fourier amplitude characteristics. However, the general reproducibility of the waveforms was worse than that of the other two earthquakes. One reason may be the phase characteristics of the EGF events. As shown in Tables 1 and 4, these mechanisms are not necessarily consistent. The small synthetic Fourier spectrum at KMM003 may have been caused by the destructive summation of the seismic waves from divided subevents. The location of KMM003 is sensitive to the number of divisions. Another important factor is the effect of near-surface rupture. This effect was also observed at KMM006. The synthetic Fourier spectrum

was underestimated at low frequencies, and the first velocity pulse in the NS direction was not reproduced by the synthetic waveform. A combined model with both large- and small-scale slip features (e.g., Pitarka et al. 2020) yields better fitting for sites near-surface ruptures.

The robustness of the prediction at KUMA for the mainshock was examined here as it was for the foreshock. The parameters were varied with the following ranges: The seismic moments of subevents 1, 2, and 3: [0.3E+18 Nm, 0.4E+18 Nm, 0.5E+18 Nm], [0.2E+18 Nm, 0.3E+18 Nm, 0.4E+18 Nm], and [0.9E+25 Nm, 1.0E+25 Nm, 1.1E+25 Nm], respectively. The rupture velocities inside the subevent: [2.3 km/s, 2.5 km/s, 2.7 km/s]. The lengths (widths) of subevents 1, 2, and 3: [2 km, 3 km, 4 km], [2 km, 3 km, 4 km] and [3 km, 4 km, 5 km], respectively. The numbers of divisions: [3, 4, 5]. The rise times were fixed to the values listed in Table 4 to restrict the number of cases. The seismic moment and length (and width) of the subevents varied independently, and the other parameters were assumed to be common to all subevents. Total of 6561 (3^8) cases were calculated and 3577 cases showed a better average FS error than the reference case. The minimum average FS error was 0.102, and the average FS error of the reference case was 0.151. The FS errors were evaluated except for KUMA. The synthetic Fourier spectra at KUMA for these cases and the reference case are shown in Fig. 14. The standard deviation of the Fourier spectra is within a factor of 1.5–2, which is almost the same as in the case of the foreshock. Again, this factor depends on the permissible FS error range (0.102–0.151 here) and should be regarded as
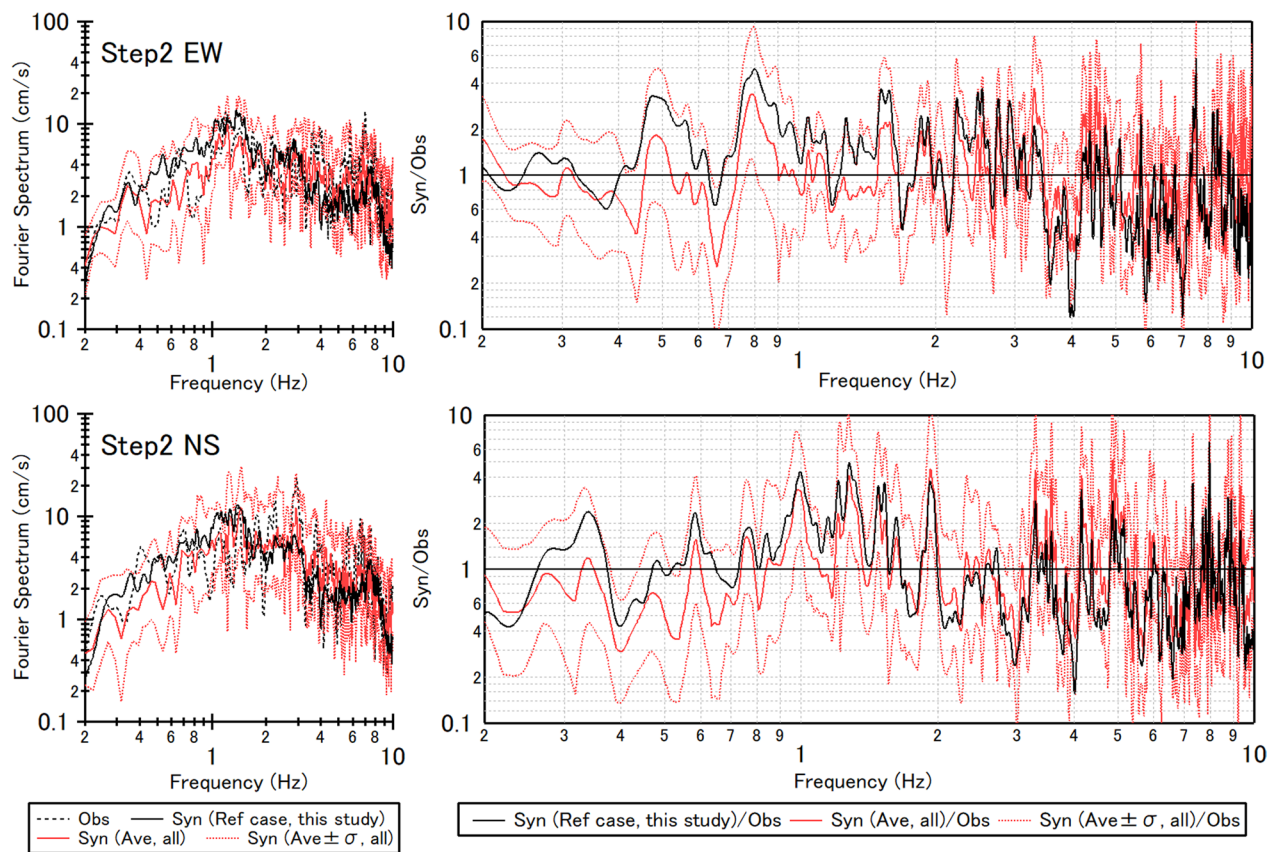
Fig. 15 Comparisons of the predictions in this study and those by blind prediction participants for the earthquake of 2016/04/16 3:03 (M_w 5.5). (Left) Black dashed and solid lines indicate the observed spectra and the synthetic spectra of the reference case, respectively. Red solid and dashed lines indicate the average and average $\pm\sigma$ spectra of all participants, respectively. (Right) Black and red lines indicate the ratio of the lines of same type in the left panel to the observed spectrum

an example value. Figure 14 also illustrates that the reference case was not intentionally adjusted for KUMA. The ranges of the FS errors are shown in Fig. 14. The FS errors in Figs. 10 and 14 show that the predictability at KUMA is comparable to that at other sites in terms of the FS error. Further case studies are required to verify whether this tendency applies to other earthquakes.

Discussions
Comparisons with other prediction methods
In the previous section, the simulation results were compared with the observed strong motion. In this section, our results are compared with those of other blind prediction participants, and the relative performance of our method is discussed. The average and standard deviation of the blind prediction participants, our results, observed spectra, and the ratio of the observed spectra for Steps 2, Step 3 foreshock, and Step 3 mainshock are shown in Figs. 15, 16, and 17, respectively. There were 18 predictions in Step 2 and 16 predictions in Step 3.

For Step 2, the average of all participants reproduced the observed spectrum well, as shown in Fig. 15. Figure 15 shows that our results were generally within one standard deviation of the results reported by all participants. The corrected EGF method performed similarly to other methods, including the 1D approach, the spectral ratio approach, and other strong ground motion methods.

For Step 3 foreshock, the average of all participants was clearly smaller than the observed spectra below 2 Hz in both the EW and NS directions as shown in Fig. 16. However, our results fluctuate around the observed spectra in this frequency range. On average, our results appear to perform well. As shown in Figs. 8, there was no underestimation in the synthetic Fourier spectra at the neighboring sites. Thus, by referring to neighboring sites, our synthetic spectra did not underestimate the observed spectra. Figure 10 also illustrates that there is no sign of underestimation in the synthetic Fourier spectra at KUMA for the various cases, indicating the robust predictability of our method for the foreshock. However, the
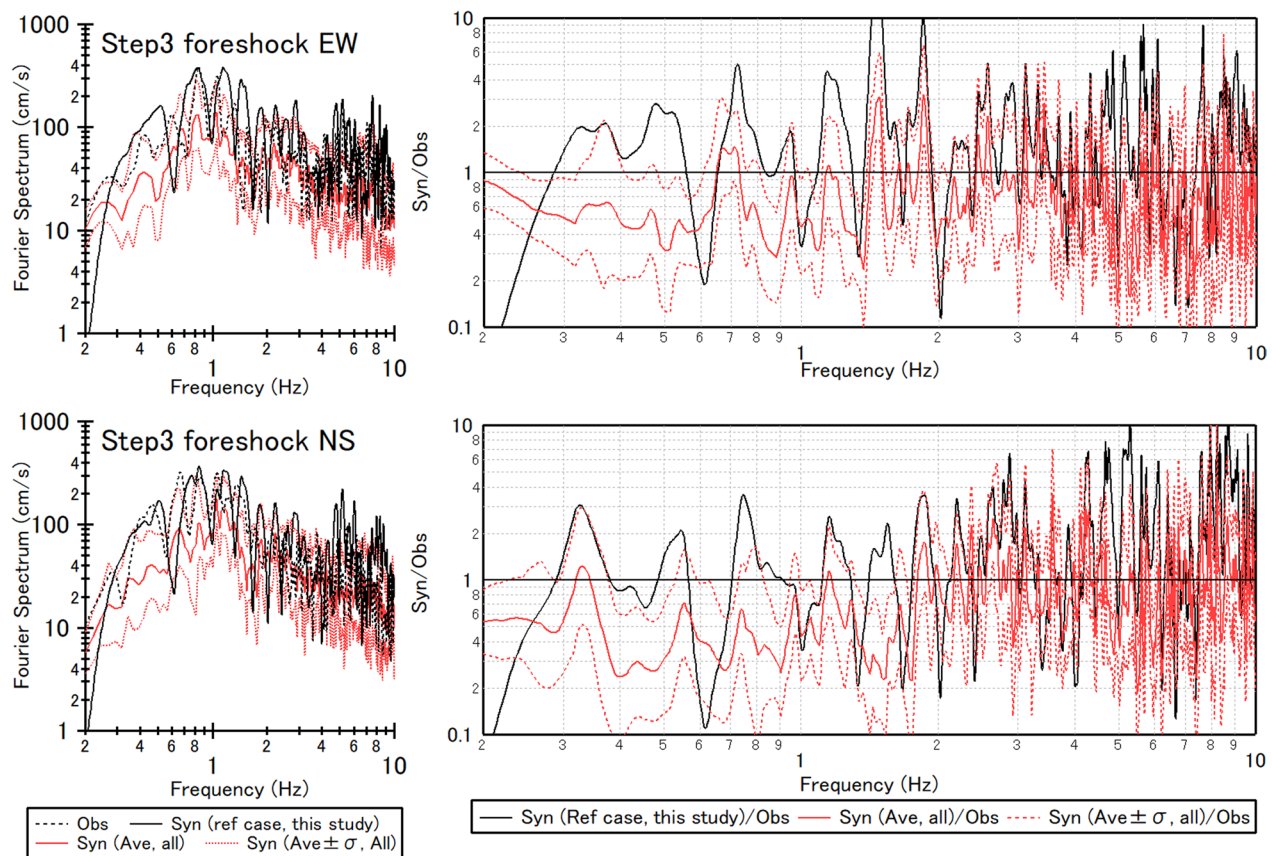
Fig. 16 Comparisons of the predictions in this study and those by other blind prediction participants for the earthquake of 2016/04/14 21:26 (M_w 6.1). (Left) Black dashed and solid lines indicate the observed spectra and the synthetic spectra of the reference case (Table 2) in this study, respectively. Red solid and dashed lines indicate the average and average $\pm \sigma$ spectra of all participants, respectively. (Right) Black and red lines indicate the ratios of the lines of same type in the left panel to the observed spectrum

fluctuation in the synthetic spectra around the observed spectra was larger than the average line shown in Fig. 16. This large fluctuation is caused by the summation process in the corrected EGF method. The synthetic Fourier spectrum has a large trough in the frequency at which the ground motions from the divided subevents are summed inconsistently. For example, reducing the fluctuation by introducing randomness in the rupture velocity leads to better and more robust predictions with the corrected EGF method.

For Step 3 mainshock, the average spectra of all participants were smaller than the observed spectra below 2 Hz, which is similar to the foreshock case. The synthetic spectra of our prediction were smaller than the observed spectra below 2 Hz and behaved similarly to the average line, particularly in the NS direction. This indicates that the prediction of large earthquakes can be improved. In the EW direction, the degree of underestimation of our result was greater than the average. This may be caused by the inconsistent summation in the frequency around 0.3–0.5 Hz. At frequencies above 2 Hz,

our prediction was larger than one standard deviation of the participants. One possible reason for this is the nonlinear site response (e.g., Sun et al. 2022). In this study, a simple nonlinear effect by Nozu et al. (2009) was used in the simulation via two parameters v_1 and v_2. The fittings at high frequencies improved if larger nonlinear effects were considered. However, it is difficult to determine these parameters with confidence without a detailed subsurface structure. Determining the nonlinear parameters is another important task to be addressed.

Prediction sensitivity to the rupture scenario

The robustness of the post-earthquake prediction was discussed. The uncertainty in the prediction of future earthquakes is examined in this section by varying the rupture scenario of the mainshock. Variations in the rupture scenario were considered based on the locations of the subevents, rupture starting points, and dip angles of the faults as shown in Table 5. The other source parameters were fixed, and the values in Table 4 were used. The rupture times of the subevents were determined by
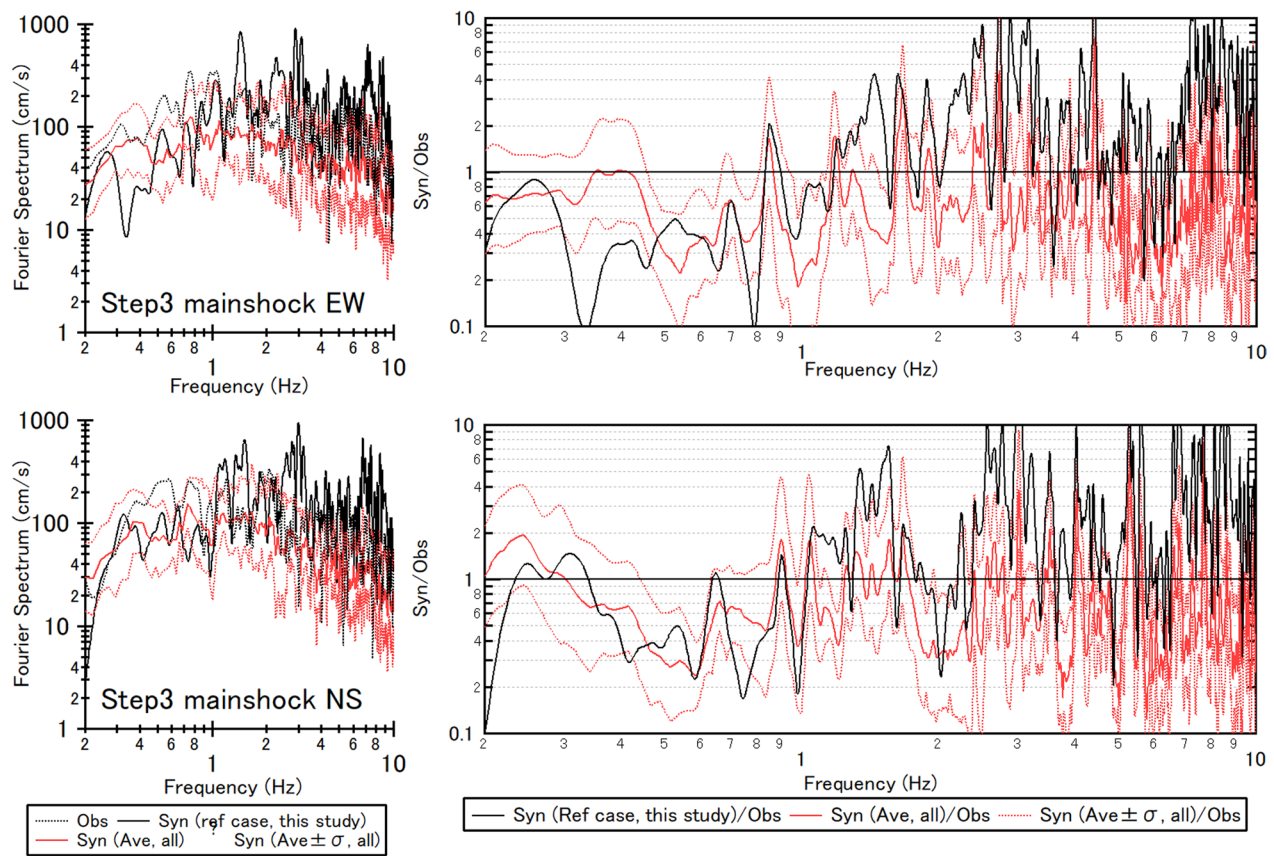
Fig. 17 Comparisons of the predictions by this study and other blind prediction participants for the earthquake of 2016/04/16 01:25 (M_w 7.1). (Left) Black dashed and solid lines indicate the observed spectra and the synthetic spectra of the reference case (Table 2) in this study, respectively. Red solid and dashed lines indicate the average and average±σ spectra of all participants, respectively. (Right) Black and red lines indicate the ratio of the lines of same type in the left panel to the observed spectrum
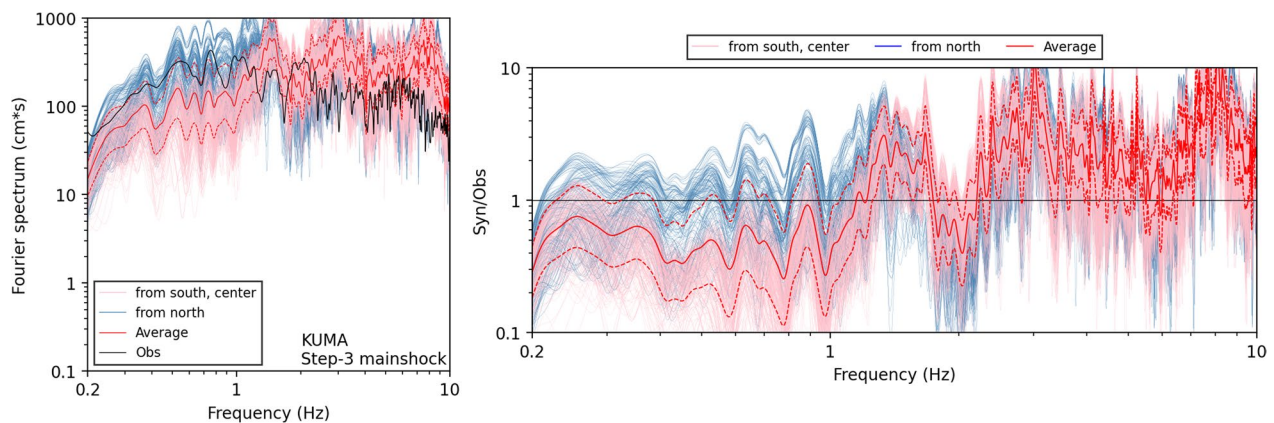
Fig. 18 Sensitivity of the prediction at KUMA to the rupture scenario. (Left) Blue and pink lines indicate the synthetic Fourier spectra of rupture scenarios that begin from the south or center (pink) and north (blue), respectively. Red solid and dashed lines indicate the average of all the rupture scenarios and the range of one standard deviation, respectively. The black line indicates the observed spectrum. (Right) Blue, pink, and red lines indicate the ratio of the lines of same type in the left panel to the observed spectrum

Table 5 Prediction sensitivity to the rupture scenario

	Number of cases	Description
Lateral location of the subevents	12	2 for subevent 1 and 6 for subevents 2 and 3
Depths of the subevents	4	Shallow and deep cases for subevent 1 and subevents 2 and 3, respectively Deep cases are as shown in Fig. 11. In shallow cases, subevents were moved by 5 km along the dip
Rupture starting point	3	Ruptures from south, center, and north were considered. Center cases start at the hypocenter of the mainshock
Dip angle	3	(Hinagu, Futagawa) = (62, 50), (72, 60), (82, 70) degrees
Total	432	

assuming a rupture propagation speed of 2.5 km/s from the first rupture point.

The synthesized and observed Fourier spectra of KUMA are shown in Fig. 18. Figure 18 indicates that the variation owing to the rupture scenario was the largest at 0.5–1 Hz. The rupture scenarios from the north clearly provide larger spectra in this frequency range than the other scenarios. This is due to the directivity effect of subevents 2 and 3. When the rupture started from the south or center, which was adopted in the reference case, KUMA was in the opposite direction to the rupture propagation of subevents 2 and 3. However, when the rupture starts from the north, KUMA was in the direction of the rupture propagation of subevents 2 and 3. Thus, this result demonstrates a large variation due to the rupture directivity effect in the simulation. Figure 18 also implies that the predictability at KUMA improved with the forward rupture directivity. Of course, there are many factors that may contribute to ground motion prediction. However, how the influence of backward/forward directivity effect appears in the observed strong motions and modeling of the directivity effect are worth investigating to improve the prediction.

Conclusions

In this article, the methods and results of strong ground motion simulations of the 2016 Kumamoto earthquake sequence are described. The main purpose of the simulations was to participate in the blind prediction exercise in ESG6 and to examine the performance of the corrected EGF method. Regional spectral inversion was conducted to determine the appropriate Q-value and site amplification factors. The observed and synthetic strong motions were compared at strong motion sites, including KUMA. Synthetic strong motions were shown to explain the strong ground motions observed at KUMA. The robustness of the prediction at KUMA was comparable to that at the other sites used in source modeling. Compared with other methods, our predictions were generally within one standard deviation of the participants and showed good agreement with the observed spectra. For the foreshock, the reproducibility of our results was good on average below 2 Hz, although a large fluctuation in the Fourier spectrum was observed. For the mainshock, our prediction and the average of the participants were both smaller than the observed spectra below 1 Hz, indicating the difficulty in predicting strong motions of a large earthquake. The uncertainty of rupture scenarios should also be considered when predicting future earthquakes. A sensitivity test of the rupture scenario indicated that the variability of the prediction was largest at the frequency at which the directivity effect was apparent. These results provide useful information for applying the corrected EGF method.

Author contributions
YN conducted all the simulations and analyses and wrote the manuscript. The author read and approved the final manuscript.

Declarations

Ethics approval and consent to participate
Not applicable.

Consent for publication
Not applicable.

Competing interests
The author declares that he has no competing interests.

Author details
[1]Engineering Seismology Group, Port and Airport Research Institute, 3-1-1 Nagase, Yokosuka, Kanagawa 239-0826, Japan.

References

Aoi S, Asano Y, Kunugi T, Kimura T, Uehira K, Takahashi N,Ueda H, Shiomi K, Matsumoto T, Fujiwara H (2020) MOWLAS: NIED observation network for earthquake, tsunami and volcano. Earth Planets Space 72:126. https://doi.org/10.1186/s40623-020-01250-x

Asano K, Iwata T (2016) Source rupture processes of the foreshock and mainshock in the 2016 Kumamoto earthquake sequence estimated from the kinematic waveform inversion of strong motion data. Earth Planets Space 68:147. https://doi.org/10.1186/s40623-016-0519-9

Boore DM (1983) Stochastic simulation of high-frequency ground motions based on seismological models of the radiated spectra. Bull Seismol Soc Am 73:1865–1894

Castro RR, Anderson JG, Singh SK (1990) Site response, attenuation and source spectra of S waves along the Guerrero, Mexico, subduction zone. Bull Seismol Soc Am 80:1481–1503

Fernández C, Nozu A, Crempien JGF, Llera JC (2021) Simulation of pulse-like ground motions during the 2015 Mw 8.3 Illapel earthquake with a new source model using corrected empirical Green's functions. Seismol Res Lett 93:76–90. https://doi.org/10.1785/0220200446

Fujiwara S, Yarai H, Kobayashi T, Morishita Y, Nakano T, Miyahara B, Nakai H, Miura Y, Ueshiba H, Kakiage Y, Une H (2016) Small-displacement linear surface ruptures of the 2016 Kumamoto earthquake sequence detected by ALOS-2 SAR interferometry. Earth Planets Space 68:160. https://doi.org/10.1186/s40623-016-0534-x

Goto H, Toyomasu A, Sawada S (2019) Delayed subevents during the Mw62 first shock of the 2016 Kumamoto, Japan, earthquake. J Geophys Res Solid Earth 124:13112–13123. https://doi.org/10.1029/2019JB018583

Irikura K (1983) Semi-empirical estimation of strong ground motion during large earthquakes. Bull Disas Prev Res Inst 33:63–104

Irikura K (1986) Prediction of strong acceleration motion using empirical Green's function. In: Proc of the 7th Japan Earthquake Engineering Symposium 151–156.

Irikura K, Kagawa T, Sekiguchi H (1997) Revision of the empirical Green's function method. In: Program and abstracts of the Seismological Society of Japan 24–26.

Irikura K, Miyakoshi K, Kamae K, Yoshida K, Somei K, Kurahashi S, Miyake H (2017) Applicability of source scaling relations for crustal earthquakes to estimation of the ground motions of the 2016 Kumamoto earthquake. Earth Planets Space 69:10. https://doi.org/10.1186/s40623-016-0586-y

Iwata T, Irikura K (1986) Separation of source, propagation and site effects from observed S-waves. Zisin 2(39):579–593

Kamae K, Irikura K (1998) Source model of the 1995 Hyogo-ken Nanbu Earthquake and simulation of near-source ground motion. Bull Seismol Soc Am 88:400–412

Kato K (2001) Evaluation of source, path, and site amplification factors from the K-NET strong motion records of the 1997 Kagoshima-Ken-Hokuseibu earthquakes. J Struct Constr Eng 543:61–68

Kawase H, Matsushima S, Nagashima F, Baoyintu NK (2017) The cause of heavy damage concentration in downtown Mashiki inferred from observed data and field survey of the 2016 Kumamoto earthquake. Earth Planets Space 69:3. https://doi.org/10.1186/s40623-016-0591-1

Kowada A, Tai M, Iwasaki Y, Irikura K (1998) Evaluation of horizontal and vertical strong ground motions using empirical site-specific amplification and phase characteristics. J Struct Construct Eng 63:97–104

Kubo H, Suzuki W, Aoi S, Sekiguchi H (2016) Source rupture processes of the 2016 Kumamoto, Japan, earthquakes estimated from strong-motion waveforms. Earth Planets Space 68:161. https://doi.org/10.1186/s40623-016-0536-8

Matsushima S, Yamanaka H, Tsuno S, Sato H, Inagaki Y (2021) Results of borehole survey at the target site of ESG6 blind prediction exercise and laboratory tests. In: Proceedings of the 6th IASPEI/IAEE International Symposium: Effects of Surface Geology on Seismic Motion, Online, 30 August-1 September 2021.

Nakano K, Matsushima S, Kawase H (2015) Statistical properties of strong ground motions from the generalized spectral inversion of data observed by K-NET, KiK-net, and the JMA shindokei network in Japan. Bull Seismol Soc Am 105:2662–2680. https://doi.org/10.1785/0120140349

Nishikiori Y, Fukunaga Y, Nozu A, Miyata M (2019) Comprehensive report for correction method of level-1 earthquake ground motion. Technical Note of National Institute for Land and Infrastructure Management 1065.

Nozu A (2012) A simplified source model to explain strong ground motions from a huge subduction earthquake—simulation of strong ground motions for the 2011 off the Pacific Coast of Tohoku Earthquake with a pseudo point-source model. Zisin2 65:45–67. https://doi.org/10.4294/zisin.65.45

Nozu A, Nagasaka Y (2017) Rupture process of the main shock of the 2016 Kumamoto earthquake with special reference to damaging ground motions: waveform inversion with empirical Green's functions. Earth Planets Space 69:22. https://doi.org/10.1186/s40623-017-0609-3

Nozu A, Nagao T, Yamada M (2006) Simulation of strong ground motions based on site-specific amplification and phase characteristics. Third International Symposium on the Effects of Surface Geology on Seismic Motion, Grenoble, France.

Nozu A, Nagao T, Yamada M (2009) Simulation of strong ground motions using empirical site amplification and phase characteristics - modification to incorporate causality -. Doboku Gakkai Ronbunshuu A, 65, 3:808–813. https://doi.org/10.2208/jsceja.65.808

Pan D, Miura H, Kanno T, Shigefuji M, Abiru T (2022) Deep-neural-network-based estimation of site amplification factor from microtremor H/V spectral ratio. Bull Seismol Soc Am 112:1630–1646. https://doi.org/10.1785/0120210300

Pitarka A, Graves R, Irikura K, Miyakoshi K, Rodgers A (2020) Kinematic rupture modeling of ground motion from the M7 Kumamoto, Japan earthquake. Pure Appl Geophys 177:2199–2221. https://doi.org/10.1007/s00024-019-02220-5

Shible H, Hollender F, Bindi D, Traversa P, Oth A, Edwards B, Klin P, Kawase H, Grendas I, Castro RR (2022) GITEC: a generalized inversion technique benchmark. Bull Seismol Soc Am 112:850–877. https://doi.org/10.1785/0120210242

Somei K, Asano K, Iwata T, Miyakoshi K, Yoshida K, Yoshimi M (2019) Source, propagation path, and site characteristics separated from strong motion records during the 2016 Kumamoto, Japan, earthquake sequence. JAEE. https://doi.org/10.5610/jaee.19.6_42

Sugito N, Goto H, Kumahara Y, Tsutsumi H, Nakata T, Kagohara K, Matsuta N, Yoshida H (2016) Surface fault ruptures associated with the 14 April foreshock (*M*ⱼ 6.5) of the 016 Kumamoto earthquake sequence, southwest Japan. Earth Planets Space 68:170. https://doi.org/10.1186/s40623-016-0547-5

Sun J, Kawase H, Fukutake K, Nagashima F, Matsushima S (2022) Simulation of soil liquefaction distribution in downtown Mashiki during 2016 Kumamoto earthquake using nonlinear site response. Bull Earthq Eng 20:5633–5675. https://doi.org/10.1007/s10518-022-01426-8

Tsuno S, Kawase H, Yamanaka H, Matsushima S, Iwata T, Hayakawa T, Ikeura T, Noguchi S, Kaneda K (2021a) Results of blind prediction Step 2: simulation

of weak motions observed at the Kumamoto test site. In: Proceedings of the 6th IASPEI/IAEE International Symposium: Effects of Surface Geology on Seismic Motion, Online, 30 August-1 September 2021a.

Tsuno S, Kawase H, Yamanaka H, Matsushima S, Iwata T, Hayakawa T, Ikeura T, Noguchi S, Kaneda K (2021b) Results of blind prediction Step 3: simulation of strong motions observed at the Kumamoto test site. In: Proceedings of the 6th IASPEI/IAEE International Symposium: Effects of Surface Geology on Seismic Motion, Online, 30 August-1 September 2021b.

Publisher's Note